# Biomarker-Mediated Disruption of Coffee-Ring Formation as a Low Resource Diagnostic Indicator

Joshua R. Trantum,[†] David W. Wright,*[‡] and Frederick R. Haselton*[†]

[†]Department of Biomedical Engineering and [‡]Department of Chemistry, Vanderbilt University VU Station B 351631 Nashville, Tennessee 37235, United States

S **Supporting Information**

ABSTRACT: The ring pattern resulting from the unique microfluidics in an evaporating coffee drop is a well-studied mass transport phenomenon generating interest in the research community mostly from a mechanistic perspective. In this report, we describe how biomarker-induced particle–particle assemblies, magnetic separation, and evaporation-driven ring formation can be combined for simple pathogen detection. In this assay design, the presence of biomarkers causes self-assembly of a magnetic nanoparticle and a fluorescently labeled micrometer-sized particle. A small spherical magnet under the center of the drop prevents these assemblies from migrating to the drop's edge while a nonreactive control particle flows to the edge forming a ring pattern. Thus the presence or absence of biomarker results in distinctly different distributions of particles in the dried drop. Proof-of-principle studies using poly-L-histidine, a peptide mimic of the malaria biomarker *pf*HRPII, show that the predicted particle distributions occur with a limit of detection of approximately 200–300 nM.
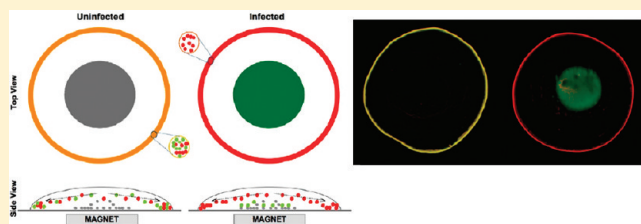
INTRODUCTION

Deegan et al. were the first to elucidate evaporation-driven capillary flow as the underlying mechanism of ring formation in a drying drop.[1−3] There have since been many studies of how various physical parameters affect ring deposition patterns, such as pinning criteria,[4] particle size,[4] solvent type,[2] surfactant effects,[5] and modeling evaporation flux,[6] microfluidic velocity vectors,[5,7,8] and imaging flow patterns.[9] Efforts to understand conditions that promote or obstruct ring patterns in colloidal drops have mostly been applied to eliminate its occurrence, which causes deleterious effects in applications as wide ranging as microarray deposition, ink jet printing, and paint manufacturing. For example, Yunker et al.[10] recently showed that sufficiently high aspect ratio ellipsoidal particles at the air–liquid interface arrests outward migration resulting in a homogeneous film deposition pattern, Bhardwaj et al.[11] demonstrated that deposition patterns can be tuned by controlling pH-dependent particle-substrate forces, and Wong et al.[12] demonstrated how the phenomenon can be used for chromatographic separation of nanosized colloidal particles. Some recent studies have also investigated pattern formation in drying drops containing biological material.[13−16] However, efforts to exploit the visual appeal of this phenomenon for disease detection have not been described.

Particles in an evaporating colloidal drop migrate to the drop's edge forming a ring on the underlying substrate. As originally described by Deegan et al., colloidal particles present at the triphase interface, i.e., the wetted contact line, are pinned to the substrate as a result of surface tension effects and substrate topological heterogeneities.[3] Maximum evaporative

flux occurs at the periphery due to greater volume of unsaturated gas into which solvent molecules can disperse. The surface tension-dependent drop geometry is then constrained by a pinned contact line, unable to recede as solvent evaporates preferentially from the edge. An internal, radial flow is established, replenishing lost solvent at the edge. Colloidal particles are transported by this flow and deposited at the edge resulting in a readily visible ring pattern (Figure 1). We hypothesize that this ring pattern can be controlled by biomarker-mediated interference of particle migration to the edge and therefore disruption of ring formation. For example, biomarker assembly of a colored particle to a magnetic iron oxide particle immobilized in the drop center by an applied magnetic field should cause a shift in the color pattern. If true, the coffee ring effect could potentially be developed as a self-contained visual indicator of biomarker-mediated binding events with potential diagnostic utility in a low resource setting.

We have chosen malaria detection as a model system for proof-of-concept studies because it has a well-identified biomarker, *Plasmodium falciparum* histidine rich protein (*pf*HRPII), and biomarker mimics are both well-characterized and readily available.[17−19] The most common malaria-causing parasite, *P. falciparum*, secretes *pf*HRPII into the serum of infected individuals at levels ranging from 10^7 to 10^{10} molecules per μL depending on the degree of parasitemia. For initial
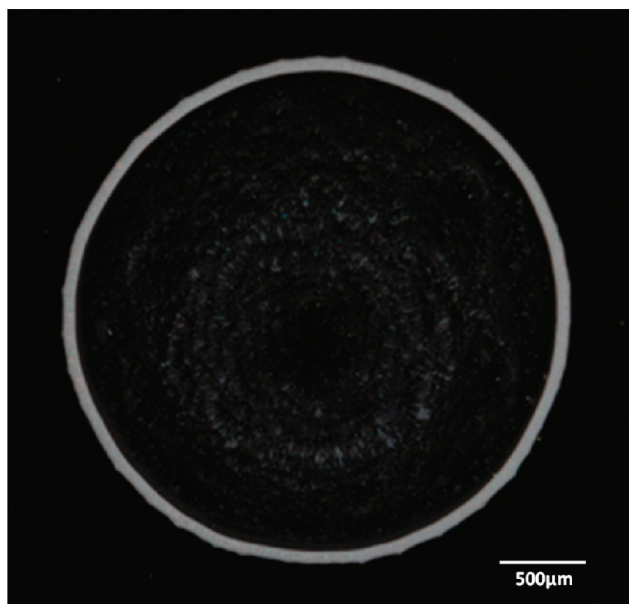
Figure 1. Photograph of the characteristic "coffee ring" particle deposition pattern after evaporation of a 3 μL drop containing 10^6 1-μm white latex particles taken with a Nikon D100 camera using an AF Micro Nikkor lens and extension tube. The drop has a diameter of approximately 3 mm.

proof-of-concept studies, we chose poly-L-histidine (PLH) as a *pf*HRPII biomimic. Our objective is to determine whether we can use the unique microfluidics present in an evaporating drop to detect the presence of biomarkers in this model system.

RESULTS AND DISCUSSION

Details of the assay design are shown in Scheme 1. A biological sample is mixed with a solution containing three different particles. Two of these particles, a magnetic particle and a biomarker indicator particle (green), have interfaces designed to interact with the disease biomarker, while a third is a nonreactive control particle (red). Biomarkers present in solution cross-link the two surface functionalized particles (magnetic and indicator) inducing self-assembly. A small volume of the particle suspension is deposited on a glass substrate centered above a magnetic field, and the nonreactive control particles (red) are transported to the edge forming a red ring. The indicator particles (green) are either transported to the edge in the absence of biomarker or magnetically pulled to the center in the presence of biomarker. The co-location of indicator (green) and control (red) particles at the edge creates a yellow ring (left panel) and indicates a negative result, while a red ring and a green center spot indicates a positive result (right panel). As Scheme 1 illustrates, the assay generates an easily interpretable pattern.

Experimentally observed changes (Figure 2) are in general agreement with the theoretical model presented in Scheme 1 (top view). In the presence of the malaria surrogate, PLH (top row), the indicator particle (green) is cross-linked to the magnetic particle and consequently pulled to the center resulting in a red ring and green center. In the absence of PLH (bottom row), both control (red) and indicator (green) particles flow to the edge creating a yellow ring leaving only magnetic particles in the drop center as seen in the corresponding phase contrast image. Poly-L-aspartic acid (PLD) is used as a negative control peptide (bottom row).

Scheme 1. Coffee Ring Assay Schematic[a]
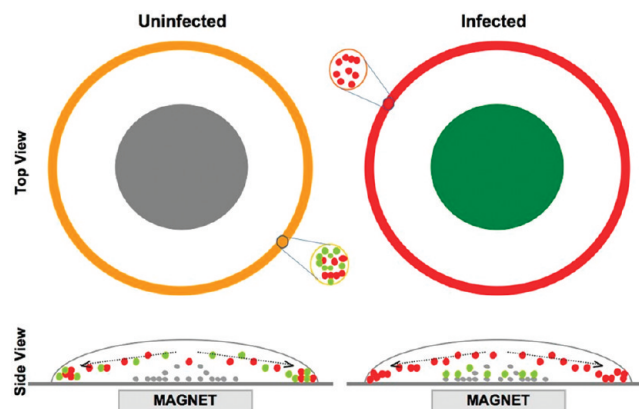
[a]As illustrated in the left panel, in the absence of biomarker, green particles are free to migrate to the edge, and the co-location of red and green particles at the edge yields a yellow ring. In the right panel, the presence of biomarker cross-links green and iron oxide particles creating a green center spot and a ring color change from yellow to red.
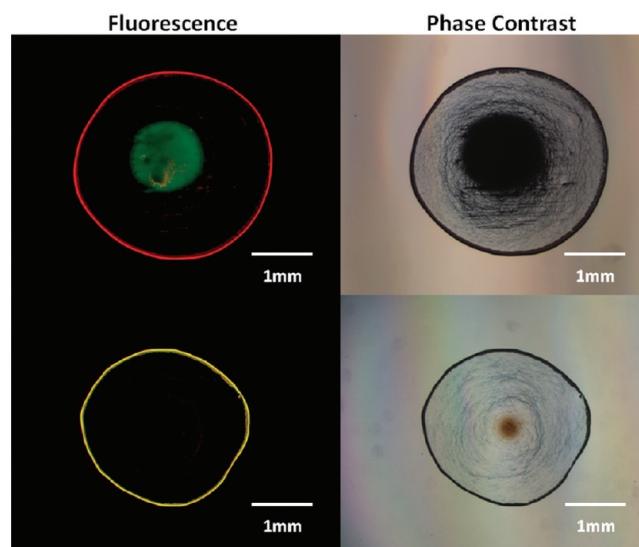
Figure 2. Fluorescence (left panels) and phase images (right panels) of particle deposition patterns observed with PLH target (top row) and PLD control (bottom row). Fluorescence images show the change in color triggered by the presence of biomarker (1.74 μM) from a red ring/green center to a yellow ring without biomarker. Phase images show that magnetic particles are concentrated in the drop center in both positive and negative assays. The center spot in the positive phase contrast image (upper right) consists of both iron oxide and green polystyrene particles resulting in a larger mass spot than the corresponding negative image (lower right).

In addition to the color changes seen in the fluorescence images, the phase images also show the change in particle distribution. The PLH (top row) phase contrast image shows a greater number of particles in the center relative to the PLD (bottom row) image as a result of magnetic particle–green particle assemblies. The PLH and PLD phase contrast images contain the same number of magnetic particles; however, the presence of the cross-linked green particle in the PLH center results in a greater number of total particles at the drop center compared to the PLD sample.

The assay demonstrates biomarker concentration dependence on peptide target (Figure 3). Images obtained with the
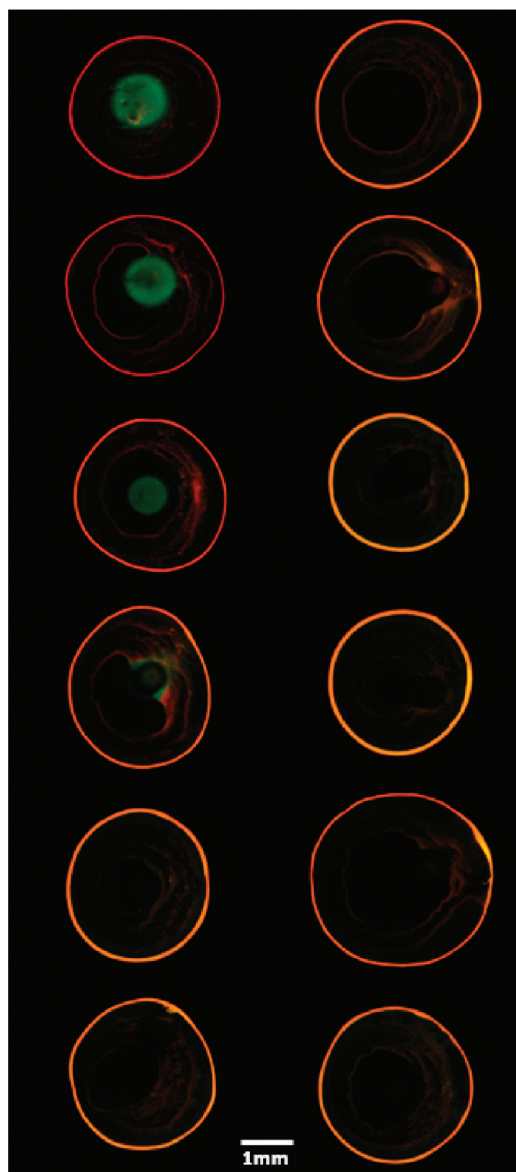

Figure 3. Change in coffee ring fluorescence images produced by a decrease in target concentration. Positive (PLH), shown in the left column, and negative (PLD), in the right column. Concentration decreases from top to bottom: 1.74 μM, 870 nM, 435 nM, 218 nM, 109 nM, 0 nM. Signal, defined as a green center and a ring color shift from orange/yellow to red, decreases with decreasing PLH concentration.

addition of PLH (+, left panels) and PLD (− control, right panels) are shown for peptide concentrations of 1.74 μM (top panels) to zero (bottom panels) using the optimized parameters determined in prior experiments (Supporting Information). At the highest concentration, the biomarker-induced pattern is similar to that observed in Figure 2. Biomarker-induced assemblies reduce the number of green indicator particles at the drop edge and increase the number of green indicator particles in the center of the drop. As shown in the left panels, decreasing PLH concentration causes the ring color to become progressively more orange/yellow in color due to co-location of a greater number of green indicator particles

and red control particles at the drop edge. A greater number of indicator particles at the drop edge reduces the number of indicator particles in the drop center, reducing the positive signal. By contrast, the color patterns of all negative samples maintain a constant orange/yellow ring appearance with no indicator particles in the drop center. At PLH concentrations below 218 nM, the positive becomes qualitatively indistinguishable from the negative, indicating the visual limit of detection for the system as currently configured. A consistent pattern similar to that observed with a PLH concentration of zero was observed at all concentrations of the nonspecific control peptide, PLD.

Quantification of the images in Figure 3 shows that the limit of detection with this design is between 200 and 300 nM. Positive and negative assay particle deposition patterns were measured under fluorescence microscopy and quantified using two different methods. Neglecting particles distributed in the drop center, signal generation at the ring was calculated by measuring the ratio of green to green+red fluorescence at the drop edge and plotted as a function of peptide concentration (Figure 4). When all indicator particles are removed from the
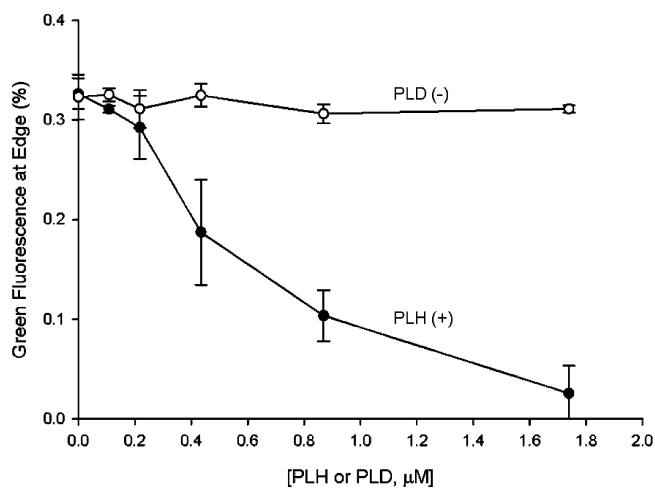
Figure 4. Edge-based signal measurement as a function of biomarker and control peptide concentrations. Green fluorescence intensity as a percentage of green + red fluorescence intensity at the ring is plotted against [PLH] (●) or [PLD] (○). $N = 3$, mean ±1 s.d.

ring, this value should approach zero. Alternatively, center signal was calculated neglecting the particles distributed at the ring by dividing the green fluorescence in the center by the nonspecific green fluorescence of the local background, i.e., the region surrounding the center spot expanding out toward but not including the ring, and plotted as a function of peptide concentration (Figure 5). This value is expected to increase with a greater number of indicator particles in the drop center.

Fluorescence signal measured at the drop's edge (Figure 4) measures disruption of indicator particle flow to the ring due to PLH-mediated cross-linking of the Ni(II)NTA ligands present on the indicator particle and magnetic particle surfaces. This metric is the ratio of green to green+red fluorescence at the drop's edge. As expected, this value decreases with increasing PLH concentration. Since the data were not normalized for differences in fluorescence quantum yield between the indicator and control particles, the PLD negative control values are fairly constant at approximately 0.33 rather than 0.5. On the basis of
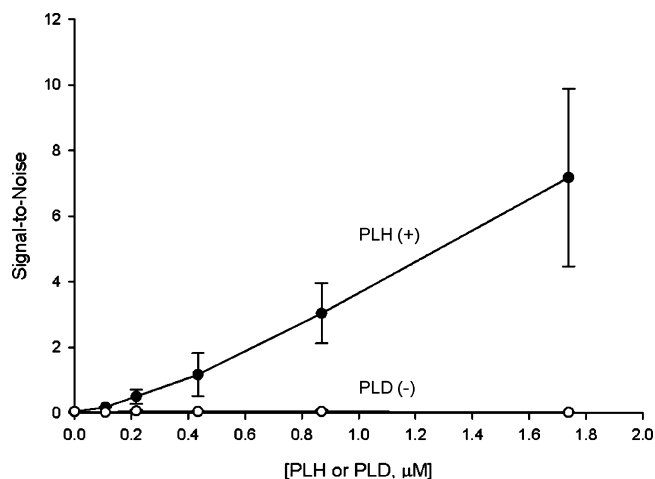
Figure 5. Center-based signal measurement as a function of biomarker and control peptide concentrations. Signal is measured as green fluorescence intensity in the center of the drop, and noise is calculated as the green fluorescence intensity difference between the two inner areas of interest. Signal-to-noise ratio is plotted against [PLH] (positive, ●) and [PLD] (negative, ○), N = 3, mean ±1 s.d.

this metric, the limit of detection is approximately 200−300 nM.

Fluorescence signal in the drop's center (Figure 5) indicates the number of indicator particles bound to magnetic particles relative to the number of indicator particles that have nonspecifically settled between the ring and the drop center. An underlying assumption in this calculation is that all green fluorescence co-located with magnetic particles is due to PLH-mediated cross-linking between indicator particles and magnetic iron oxide particles. Consistent with the assay image appearance, center signal increases with increased PLH concentration but remains constant at approximately zero in the corresponding negative (PLD) assay. This center-based metric also indicates an assay limit of detection of 200−300 nM.

The two metrics quantify two ways in which the assay color distribution can be perceived and a positive and negative test result discriminated: a change in edge color and a change in the color of the drop's center. The edge-based metric plotted in Figure 4 identifies a positive result by the number of indicator particles relative to control particles in the drop ring and therefore a change in ring color. Conversely, the underlying assumption of the center-based metric (Figure 5) is that positive signal is generated when magnetic particle-indicator particle assemblies are concentrated in the drop center appearing as a green fluorescent spot. Excluding nonspecific particle-substrate binding affects, the indicator particle either migrates to the edge (no biomarker) or becomes magnetically trapped in the center (with biomarker). Although the two methods of measuring assay signal are not strictly independent, PLH concentration-dependent signal generation shown in

Scheme 2. Surface Chemistry and Particle−Particle Interactions[a]
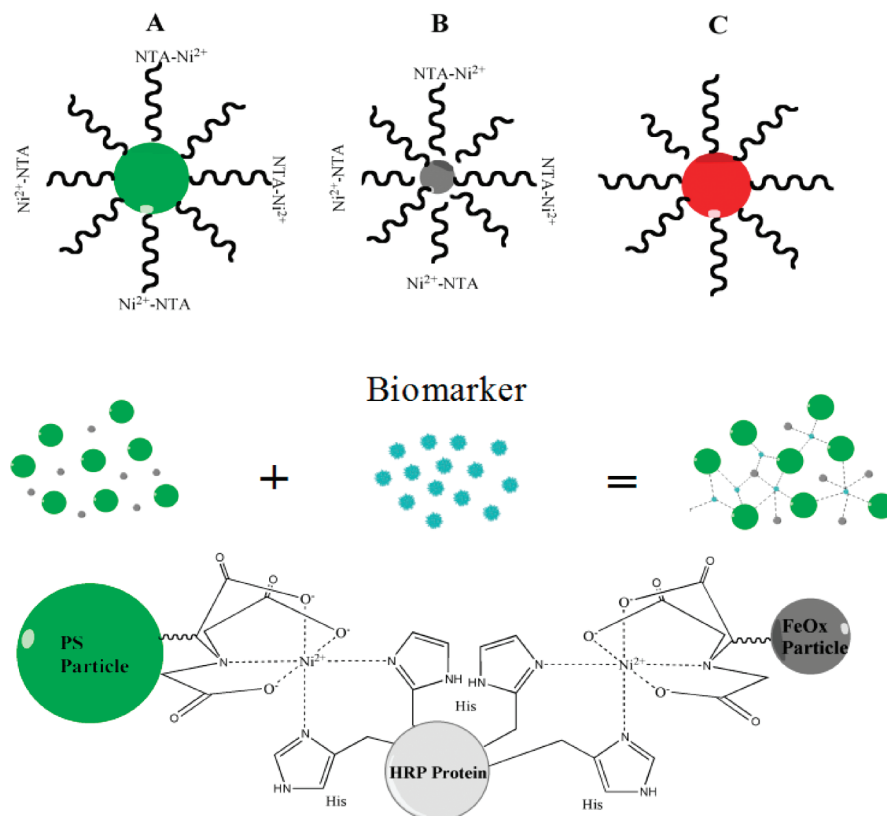
[a]Upper panel. The assay consists of three particles: (A) 1μm diameter green fluorescent polystyrene; (B) 250 nm diameter iron oxide; (C) 1μm diameter red fluorescent polystyrene. Particle (A) is surface modified with PEG and terminated with Ni(II)NTA. Particle (B) is surface modified with dextran and terminated with Ni(II)NTA. Particle (C) is pegylated. Center panel. Histidine residues in the biomarker cross-link particles (A) and (B). Lower panel. Ni(II)NTA coordinates biomarker histidines.

Figure 4 is corroborated by and consistent with results shown in Figure 5.

The particle−biomarker interface is a critical design feature that affects the particle deposition patterns shown in Figures 2 and 3. The interface employed in this study (Scheme 2) is Ni(II) nitrilotriacetic acid (NTA) chelation, a common method for isolating and purifying histidine-tagged proteins.[20,21] The Ni(II)NTA ligand is the target recognition element that induces particle aggregation in the presence of *pf*HRPII (Figure 3). PLH mimics the metal binding characteristics of *pf*HRPII, a 67 kDa protein containing 54 histidine dimer repeats conducive to metal-ion coordination. In this model system, the intrinsic metal reactivity of *pf*HRPII is the basis for biomarker-mediated particle self-assembly. This aspect has been recently demonstrated by Swartz et al. who showed that *pf*HRPII concentration-dependent aggregation of Ni(II)NTA-functionalized gold and silver nanoparticles induced a shift in surface plasmon resonance.[22] Additionally they showed the same aggregation-inducing effect using PLH and BNTII,[18] another *pf*HRPII biomimic.

The surface of the indicator particle was functionalized with Ni(II)NTA following modified procedures originally developed by Nolan et al.[23] A polyethylene glycol (PEG) spacer was incorporated between the particle surface and the NTA ligand to minimize nonspecific interactions caused by the hydrophobic particle surface. Both the indicator and magnetic particles were charged with Ni(II). The control particle was surface-modified with methyl-terminated PEG to minimize nonspecific interactions. Many different particle-biomarker interfaces could be used in this assay design. For example, antibody/antigen, phage selective binding, avidin/biotin, aptamer/antigen, or metal chelate/histidine coordination could all be developed to target a biomarker of interest. This design flexibility allows the particles to bind to a wide variety of different biomarkers and therefore potentially enables diagnostic utility for a number of diseases.

In this proof-of-concept study, the data presented (Figures 3, 4, and 5) suggest a limit of detection in the 200−300nM range, which is somewhat higher than current rapid diagnostic tests. The World Health Organization's recommended sensitivity of 2000 parasites/μL corresponds to an approximate *pf*HRPII concentration near 1nM.[24−27] Recent research has determined that currently available rapid diagnostic tests can detect *pf*HRPII concentrations as low as 800pM to 20nM *pf*HRPII.[28] Assuming that PLH suitably mimics *pf*HRPII nickel binding behavior, the detection limit of the proposed assay is approximately 1 order of magnitude above the biologically relevant *pf*HRPII concentration. We anticipate that with design enhancements, the limit of detection can be improved.

In theory, the detection limit of this approach can be improved by 6 orders of magnitude. If we conservatively assume that all indicator particles (green) in the top left panel of Figure 3 are at the drop center for a biomarker concentration of 1.74 μM, we can use this observation and the number of indicator particles present in the drop (10^6) to estimate how many biomarkers would be theoretically required to produce this image. At the theoretical limit of detection, each indicator particle is brought from the edge into the drop center by one and only one biomarker. If this were achieved experimentally, then the panel in Figure 3 (top left) would correspond to 1.74pM, well within the acceptable limits for malaria detection. Controlling the number of binding sites per particle is one potential strategy to approach the theoretical limit of detection.

Drop size is another critical design consideration affecting multiple aspects of assay performance. The effect of drop size on pattern formation in evaporating drops has been previously observed. For example, Deegan et al. empirically demonstrated that ring width scales linearly with drop radius for a given initial particle concentration.[1] Therefore, a larger drop volume generates a wider ring that facilitates visual interpretation of the assay. In the format described here, maximum drop volume is constrained by both evaporation time, which affects time-to-result, and the magnetic field strength, which decreases with increasing distance from the drop's center. The 3 μL drops fully evaporated within approximately 20 min (ambient conditions: approximately 25 °C, 30% relative humidity). This evaporation time represents a time-to-result that is consistent with that achieved with commercially available tests used to diagnose malaria in low resource environments.[29] Drop volumes larger than 3 μL may require an evaporation time that is less desirable compared to currently available diagnostic technologies (Supporting Information).

As drop volume increases, a greater magnetic field is required to pull the iron oxide particles to the drop's center. Iron oxide particles change position in the drying drop due to a time-dependent net force, the dominant components of which include the outward force caused by evaporation-induced radial flow and the inward-directed magnetic force. In order to separate particle assemblies from control particles at the drop perimeter, the magnetic force must sufficiently exceed the force caused by evaporation-induced radial flow. The magnitude of the magnetic force experienced by the iron oxide particles is a function of both the particles' magnetic susceptibility and the magnetic field strength. The iron oxide particles used in this study have a magnetic susceptibility of 43emu/g of particles (H-field = 1000 Oe). The small spherical magnet employed in this preliminary design generated a field strength of 17 mT at the drop perimeter when the poles were aligned orthogonally to the substrate. Under the influence of this magnetic field, iron oxide particles near the contact line migrate toward the drop's center with an average velocity of 80 μm/s within 10 s after the drop is deposited over the spherical magnet. All iron oxide particles are pulled to the drop's center within 30 s of applying the magnet. With no magnet present, iron oxide particles exhibit almost no radial flow within the first 10 s of drop evaporation. Outward radial flow of iron oxide particles increases as the drying process progresses reaching an average radial velocity of 6 μm/s at 6.5 min into evaporation. The inward magnetic-driven velocity occurs immediately upon drop deposition and at a rate that is at least an order of magnitude greater than the outward radial flow that occurs later in the evaporation process without the magnet present. The maximum distance iron oxide particles can be from the drop's center and still experience sufficient magnetic force to migrate to the drop's center is approximately 5.5 mm, which corresponds to a drop volume of 40 μL. These data suggest that the drop size used in this study was well within the size required for the magnet to effectively attract magnetic particle assemblies, but that larger drop volumes could also be used given a sufficiently long evaporation time.

Additional assay design features expected to impact assay performance include a larger particle radius and enhanced image analysis. For a fixed number of biomarkers, a larger particle would be expected to improve the limit of detection by producing a greater change in visual appearance. Employing automatic pattern recognition and image processing techniques,

such as those described by Kim et al.,[30] may further improve assay performance.

Optimizing the number of Ni(II)NTA ligands per particle, drop size, and particle radius will be particularly important for developing a version of this assay that has an improved limit of detection and uses colorimetric rather than fluorescent particles to enable simple visual interpretation.

■ CONCLUSION

This work demonstrates a prototype diagnostic assay based on the mechanism that causes a ring to form in an evaporating coffee drop. In the presence of a biomarker, a positive result produces a ring and center color pattern in an evaporated drop that is easily distinguished from a negative result. The difference in visual appearance is caused by biomarker-mediated disruption of particle migration to the edge producing a red ring and a green center signal, while a negative result produces a yellow ring with no center signal. This method is potentially well-suited for low-resource applications that require a simple-to-use, low cost method for pathogen detection.

■ EXPERIMENTAL METHODS

Particle Functionalization. *PEGylation.* Carboxylated polystyrene beads, mean diameter 0.97 μm, were obtained from Bang's Laboratories with two different fluorescence excitation/emission profiles: 540/600 and 480/520. The beads were washed by centrifugation three times (4.6 g) and resuspended in phosphate-buffered saline (PBS; pH 7.2) at stock concentration (1.975×10^{10} per mL). Particles were made sulfhydryl reactive by coupling *N-β*-maleimidopropionic acid hydrazide (BMPH, Fisher Scientific) via 1-ethyl-3(3-dimethylaminopropyl) carbodiimide (EDC, Sigma Aldrich). The BMPH was dissolved in PBS (pH 7.2) and added to the particle suspension at a 10-fold molar ratio to carboxyl sites. EDC dissolved in 100 mM 2-(*N*-morpholino)ethanesulfonic acid (MES) buffer (pH 4.9) was immediately added to the reaction volume to yield a 50-fold molar excess relative to carboxyl sites. The reaction volume was incubated for at least 2 h. Particle suspensions were then washed three times via centrifugation and resuspended in PBS (pH 7.2). The red control particles were pegylated by reacting with thiol-PEG-methyl (Quanta Biodesign Ltd.) dissolved in PBS (pH 7.2) to yield a 10-fold molar excess relative to maleimide groups. The suspension was incubated for at least 2 h, washed three times via centrifugation, and resuspended in deionized water. The green particle suspension was reacted with thiol-PEG-carboxylic acid (Quanta Biodesign Ltd.) dissolved in PBS (pH 7.2). The suspension was incubated for 2 h, washed three times via centrifugation, and resuspended in MES buffer (pH 4.9).

Conjugation of NTA to Polystyrene Particles. EDC and *N*-hydroxysulfosuccinimide (NHS, Sigma Aldrich) were together dissolved in MES buffer (pH 4.9) at a molar ratio of 1:2.5. The EDC/NHS solution was added to the reaction volume (in MES) to yield a 10-fold molar excess of EDC to carboxyl sites. The solution reacted for 15 min at room temperature, washed three times via centrifugation, and resuspended in PBS (pH 7.4). A solution of NTA (Sigma Aldrich) in PBS (pH 7.2) was added to yield a 10-fold molar excess relative to active sites. The reaction volume reacted for 2 h, washed via centrifugation, and resuspended in 100 mM HEPES buffer (pH 7.2).

Ni²⁺ Charging of Polystyrene-PEG-NTA Particles. Nickel chloride was dissolved in deionized water and added to the PEG-NTA-conjugated particles in 100 mM HEPES buffer (pH 8) to yield a 10-fold nickel molar excess over NTA groups. The reaction volume reacted for 2 h, was washed five times via centrifugation, and was resuspended in deionized water.

Ni²⁺ Charging of Iron Oxide-NTA Particles. Dextran-stabilized iron oxide particles having a mean diameter of 250 nm and surface-modified with NTA were obtained from Micromod Gmbh. The particles were washed three times via magnetic separation (or centrifugation) and resuspended in deionized water (0.2% Tween 20) at stock concentration (4.9×10^{11} per mL). Nickel chloride was dissolved in deionized water and added to the iron oxide-NTA particles to yield a 10-fold nickel molar excess over NTA groups. The reaction volume reacted for 2 h, was washed five times via centrifugation, and was resuspended in deionized water.

Particle Characterization. Particle concentration and size distributions of polystyrene particles were measured using a Beckman Coulter Multisizer 3 coulter counter. One microliter of stock particles was diluted in 20 mL of Isoton II diluent (Beckman Coulter) and measured using a 30 μm aperture. Iron oxide particle size distribution was measured using dynamic light scattering (Malvern Zetasizer NanoZS) by diluting 20 μL of stock particle solution in 1 mL deionized water. Polystyrene and iron oxide particle surface modification was verified by measuring zeta potentials (Malvern Zetasizer NanoZS) of the functionalized particles versus non-functionalized. For all zeta potential measurements, 20 μL of particles were diluted in 1 mL of 1 mM aqueous NaCl (pH 7.76). Nickel coordination to the NTA ligand was verified by inductively coupled plasma optical emission spectroscopy (ICP-OES). Nickel was stripped from the NiNTA functionalized particles following two-hour incubation in 2% nitric acid. Particles were removed from the nitric acid via a 2 μm syringe filter. Nickel content was measured on an Optima 7000 ICP-OES.

Experimental Protocol. The green PS-PEG-NiNTA particle (3.86×10^6 per μL in H$_2$O) was mixed 1:1 with the magnetic nanoparticle (1×10^7 per μL in H$_2$O). PLH or PLD was then added at a given concentration. Six concentrations of target or control were assessed: 1.74 μM, 870 nM, 435 nM, 218 nM, 109 nM, 0 nM. Following 30 min incubation at room temperature, the red particle (3.86×10^6 per μL) was added to the reaction volume in equal part to the other components. Particle concentrations were determined based on the number required to generate a visible ring and the optimal signal-to-noise output at [target] = 435nM (Supporting Information). A glass slide was cleaned in an acid wash containing 70% ethanol/30% hydrochloric acid (1N) for 2 h, rinsed with deionized water, and dried under nitrogen gas. A 3 μL drops were deposited in triplicate on the slide, each centered over a 3 mm spherical magnet (neodymium magnet with 179 mT field strength, Engineered Concepts) with the magnetic pole oriented orthogonal to the slide. Upon complete evaporation, the deposition patterns were imaged under fluorescence microscopy (Nikon TE2000U inverted fluorescence microscope), fluorescence intensity in predefined areas of interest (Supporting Information) was measured using Image Pro software (v7). Due to position variability during manual drop deposition the location of settled magnetic particles relative to the ring varied from drop to drop. Areas of interest (AOI) in the software program were therefore manually moved to the appropriate location in the image prior to taking the measurement. Total and mean intensities (green channel only) were recorded. Mean background noise was subtracted from each respective area of interest, and the signal metric was calculated as $f_{center}/f_{ring-center}$ (where f = background-adjusted fluorescence intensity). The three calculations were averaged per data point. The experiment was conducted in triplicate and signal values averaged and plotted. In addition to center signal, a ring signal calculation was made by measuring the green fluorescence intensity in the ring as a percentage of total ring fluorescence intensity (green + red).

Particle Tracking. The relationship between magnetic field strength and iron oxide particle motion was quantified by tracking the velocity of individual iron oxide particles near the drop perimeter both with and without the magnet in place. Colloidal suspensions in water were prepared using the same particle types and concentrations as described above. Deionized water was added to the suspension in place of the PLH or PLD solutions that were added according to the sample preparation described in the Experimental Protocol section. Three microliter volumes were deposited on a clean glass slide and centered over the magnetic field. Videos of particle motion were recorded using a 20× objective on a Nikon TE2000U inverted microscope with a charge coupled device (CCD) camera (Hamamatsu Photonics model C7780-20). Individual particle motion was tracked

using Image Pro software (v.7). Average particle velocity was calculated from the motion of 10 particles tracked over a period of 5 s. Magnetic field strength was measured at the drop perimeter with a gaussmeter (LakeShore, model 421).

A similar experiment was conducted using the same particle types, particle concentrations, and magnet but with larger drop volumes to determine the approximate drop volume and radius at which iron oxide particles at the perimeter do not migrate to the drop's center. After a sample volume was deposited on a clean glass slide, iron oxide particles at the drop's perimeter were tracked as the magnet was placed at the drop's center. The experiment was repeated for drop volumes ranging from 10 to 40 μL.

■ ASSOCIATED CONTENT

ⓢ Supporting Information

Contents include (1) methodology for determining particle count required for ring visualization, (2) figure showing areas of interest used in fluorescence intensity measurements, (3) methodology for determining particle concentrations, and (4) experimental methods and data for relating drop volume to evaporation time. This information is available free of charge via the Internet at http://pubs.acs.org/.

■ AUTHOR INFORMATION

Corresponding Author

*(F.R.H.) E-mail: Rick.Haselton@vanderbilt.edu; tel: 615-322-6622; fax: 615-343-7919. (D.W.W.) Mailing address: Vanderbilt University, Department of Chemistry, VU Station B 351822 Nashville, TN 37235.

■ ACKNOWLEDGMENTS

■ REFERENCES

(1) Deegan, R. D. *Phys. Rev. E* **2000**, *61*, 475−485.

(2) Deegan, R. D.; Bakajin, O.; Dupont, T. F.; Huber, G.; Nagel, S. R.; Witten, T. A. *Phys. Rev. E* **2000**, *62*, 756−765.

(3) Deegan, R. D.; Bakajin, O.; Dupont, T. F.; Huber, G.; Nagel, S. R.; Witten, T. A. *Nature* **1997**, *389*, 827−829.

(4) Sangani, A. S.; Lu, C. H.; Su, K. H.; Schwarz, J. A. *Phys. Rev. E* **2009**, *80*.

(5) Hu, H.; Larson, R. G. *Langmuir* **2005**, *21*, 3972−3980.

(6) Hu, H.; Larson, R. G. *J. Phys. Chem. B* **2002**, *106*, 1334−1344.

(7) Hu, H.; Larson, R. G. *Langmuir* **2005**, *21*, 3963−3971.

(8) Harris, M. T.; Widjaja, E. *AIChE J.* **2008**, *54*, 2250−2260.

(9) Kajiya, T.; Kaneko, D.; Doi, M. *Langmuir* **2008**, *24*, 12369−12374.

(10) Yunker, P. J.; Still, T.; Lohr, M. A.; Yodh, A. G. *Nature* **2011**, *476*, 308−311.

(11) Bhardwaj, R.; Fang, X. H.; Somasundaran, P.; Attinger, D. *Langmuir* **2010**, *26*, 7833−7842.

(12) Wong, T. S.; Chen, T. H.; Shen, X. Y.; Ho, C. M. *Anal. Chem.* **2011**, *83*, 1871−1873.

(13) Tarasevich, Y. Y.; Pravoslavnova, D. M. *Eur. Phys. J. E* **2007**, *22*, 311−314.

(14) Tarasevich, Y. Y.; Pravoslavnova, D. M. *Tech. Phys.* **2007**, *52*, 159−163.

(15) Larson, R. G.; Lopez, M. A.; Lim, D. W.; JLahann, J. *MRS Proc.* **2010**, *1273*.

(16) Brutin, D.; Sobac, B.; Loquet, B.; Sampol, J. *J. Fluid Mech.* **2011**, *667*, 85−95.

(17) Wright, D. W.; Ziegler, J. *Abstr. Pap. Am. Chem. Soc.* **1998**, *216*, U277−U277.

(18) Ziegler, J.; Chang, R. T.; Wright, D. W. *J. Am. Chem. Soc.* **1999**, *121*, 2395−2400.

(19) Marletta, M. A.; Schneider, E. L. *Biochemistry* **2005**, *44*, 979−986.

(20) Terpe, K. *Appl. Microbiol. Biotechnol.* **2003**, *60*, 523−533.

(21) Mori, S.; Takahashi, H. K.; Yamaoka, K.; Okamoto, M.; Nishibori, M. *Life Sci.* **2003**, *73*, 93−102.

(22) Swartz, J. D.; Gulka, C. P.; Haselton, F. R.; Wright, D. W. *Langmuir* **2011**, in press.

(23) Lauer, S. A.; Nolan, J. P. *Cytometry* **2002**, *48*, 136−145.

(24) Minigo, G.; Woodberry, T.; Piera, K. A.; Salwati, E.; Tjitra, E.; Kenangalem, E.; Price, R. N.; Engwerda, C. R.; Anstey, N. M.; Plebanski, M. *PLoS Pathog.* **2009**, *5*.

(25) Dondorp, A. M.; Desakorn, V.; Pongtavornpinyo, W.; Sahassananda, D.; Silamut, K.; Chotivanich, K.; Newton, P. N.; Pitisuttithum, P.; Smithyman, A. M.; White, N. J.; Day, N. P. J *PLoS Med.* **2005**, *2*, 1047−1047.

(26) Rajasekariah, G. H.; Martin, S. K.; Awinda, G.; Waitumbi, J.; Kifude, C. *Am. J. Trop. Med. Hyg.* **2009**, *80*, 516−522.

(27) Waitumbi, J. N.; Kifude, C. M.; Rajasekariah, H. G.; Sullivan, D. J.; Stewart, V. A.; Angov, E.; Martin, S. K.; Diggs, C. L. *Clin. Vaccine Immunol.* **2008**, *15*, 1012−1018.

(28) Reyburn, H.; Mbakilwa, H.; Mwangi, R.; Mwerinde, O.; Olomi, R.; Drakeley, C.; Whitty, C. J. *BMJ [Br. Med. J.]* **2007**, *334*, 403.

(29) WHO *Malaria Rapid Diagnostic Test Performance: Results of WHO Product Testing of Malaria RDTs: Round 3 (2010−2011)*;World Health Organization: Geneva, Switzerland, 2011.

(30) Kim, N.; Li, Z.; Hurth, C.; Zenhousern, F.; Chang, S.-F.; Attinger, D. *Anal. Methods* **2011**, in press.